

Simulation of the deformation texture of a 17%Cr ferritic stainless steel using the texture component crystal plasticity finite element method considering texture gradients

I. Tikhovskiy, D. Raabe ^{*}, F. Roters

Max-Plank-Institut für Eisenforschung, Department Microstructure Physics and Metal Forming, Max-Planck-Straße 1, D-40237 Düsseldorf, Germany

Received 6 October 2005; received in revised form 25 November 2005; accepted 20 December 2005

Available online 25 January 2006

Abstract

We use a texture component crystal plasticity finite element method for the simulation of plane strain compression (maximum thickness reduction 95%) of a ferritic stainless steel (X6Cr17, AISI 430, 1.4016). The method incorporates the graded hot band texture of the starting material and predicts the development of the orientation distribution during forming in the surface and in the center layer considering 24 slip systems ($\{110\}\langle111\rangle$, $\{112\}\langle111\rangle$). The results are compared to experiments.

© 2006 Acta Materialia Inc. Published by Elsevier Ltd. All rights reserved.

Keywords: Anisotropy; Crystal plasticity FEM; Metal forming; Texture; bcc

1. Introduction

Ferritic stainless steels form a prominent group of construction and functional materials owing to their favorable combination of mechanical properties and corrosion resistance [1]. An important problem in the industrial processing and the final properties of these materials is the inhomogeneity of the texture through the thickness of the cold rolled and recrystallized sheets [2–6]. Detailed experimental texture studies have shown that these pronounced through-thickness texture gradients are due to texture inheritance from the preceding hot rolling procedure [7–19]. Factors such as roll-gap geometry, including the geometrical changes during a rolling pass, friction between the roll and the sheet contact surface, and the temperature gradients during hot rolling can give rise to non-homogeneous through-thickness strain fields and, as a consequence, to different hot rolling textures in different through-thickness layers [2,5,7] entailing also inhomogeneous strength and deep drawing properties of the final

product. Furthermore, through-thickness texture gradients have been linked to the phenomenon of ridging in ferritic stainless steels [20–30]. Corresponding correlation studies have revealed that sheets with stronger texture gradients are more prone to showing pronounced ridging.

Thin strip casting as opposed to conventional hot rolling before cold rolling and final recrystallization annealing has turned out to be an alternative processing route which entails superior sheet properties including negligible through-thickness and smaller in-plane texture gradients when compared to conventionally processed material [31–36].

Owing to these different aspects associated with texture inheritance in ferritic stainless steels a reliable texture simulation of forming processes of ferritic steels which takes into account through-thickness texture gradients of the hot band sheet is an essential challenge when optimizing these materials.

The aim of this study, therefore, is improving the prediction of the texture evolution during cold rolling of hot rolled ferritic stainless steel (X6Cr17) using the texture component crystal plasticity finite element method (TCCP-FEM) with 24 slip systems. This method works by using spherical orientation components for the texture

^{*} Corresponding author. Tel.: +49 2 11 67 92 268.

E-mail address: raabe@mpie.de (D. Raabe).

approximation instead of sets of single orientations. More details on that are given in the ensuing section and in Refs. [37–45]. The measured texture of a hot band steel sheet, fitted by using the texture component method, was used as starting texture for the FE calculation. In order to take the initial texture heterogeneity of the hot band sheet into account in the simulation, a simplified through-thickness texture gradient was mapped in the FE model. The simulation results are compared to experimental data and to earlier literature data of through-thickness texture gradients observed in rolled sheets of ferritic stainless steels [2,10,11,14,19].

2. The texture component crystal plasticity finite element method

The main task of the texture component crystal plasticity FE concept is to represent sets of spherical Gaussian orientation components [46–49] on the integration points of a FE mesh for a crystal plasticity simulation. The procedure works in two steps: first, for each texture component its center orientation is assigned to each integration point. In the second step, this discrete central orientation of each of the thus mapped Gaussian distributions is at each integration point systematically re-oriented so that the resulting overall distribution reproduces the texture function which was originally prescribed. After this mapping procedure the texture simulation is conducted in the form of a conventional crystal plasticity FE model according to the approach of Kalidindi et al. [50]. Details are given in Refs. [37–45].

3. Crystallographic textures of rolled body-centered cubic metals

Owing to the cubic symmetry of the body-centered cubic (bcc) crystal system and the orthorhombic sample system, which is set-up by the rolling (RD), normal (ND), and transverse directions (TD) of the sample, textures of rolled bcc polycrystals are typically presented in the reduced Euler space where an orientation is given by the three Euler angles φ_1 , Φ and φ_2 , ($0^\circ \leq \varphi_1, \Phi, \varphi_2 \leq 90^\circ$). We use the Bunge–Euler notation throughout this article [51]. Crystal orientations can also be conventionally described by the use of Miller indices $\{hkl\} \langle uvw \rangle$, where $\{hkl\}$ describes the crystal plane parallel to the sheet surface and $\langle uvw \rangle$ the crystal direction parallel to RD. Important texture components for bcc steels are located on the α_{bcc} -fiber (fiber axis $\langle 110 \rangle$ parallel to the rolling direction, RD, including major components $\{001\}\langle 110 \rangle$, $\{112\}\langle 110 \rangle$, and $\{111\}\langle 110 \rangle$), γ -fiber (fiber axis $\langle 111 \rangle$ parallel to the normal direction, ND, including major components $\{111\}\langle 110 \rangle$ and $\{111\}\langle 112 \rangle$), η -fiber (fiber axis $\langle 001 \rangle$ parallel to RD including major components $\{001\}\langle 100 \rangle$ and $\{011\}\langle 100 \rangle$), ζ -fiber (fiber axis $\langle 011 \rangle$ parallel to ND including major components $\{011\}\langle 100 \rangle$, $\{011\}\langle 211 \rangle$, $\{011\}\langle 111 \rangle$, and $\{011\}\langle 011 \rangle$), ε -fiber (fiber axis $\langle 011 \rangle$

parallel to the transverse direction, TD, including major components $\{001\}\langle 110 \rangle$, $\{112\}\langle 111 \rangle$, $\{111\}\langle 112 \rangle$, and $\{011\}\langle 100 \rangle$), and θ -fiber (fiber axis $\langle 001 \rangle$ parallel to ND including major components $\{001\}\langle 100 \rangle$ and $\{001\}\langle 110 \rangle$) [2,19].

4. Experimental procedures

4.1. Material, texture and metallography

The study was carried out using the ferritic stainless low carbon steel X6Cr17 (AISI 430/1.4016) with a hot band thickness of 1 mm (Table 1). Since textures of ferritic steels often vary through the sample thickness [2–13], the texture of the hot band was investigated at the surface and in the center layers. The actual layer position is described by the parameter s , which indicates the distance between the actual layer inspected and the sample center layer divided by the half thickness ($s = 1.0$ surface, $s = 0.0$ center). The samples were etched prior to the measurement using HF to remove a surface layer of 15 μm . All textures have been examined by measuring the three pole figures $\{110\}$, $\{200\}$, and $\{211\}$ using $\text{CuK}\alpha_1$. From the pole figures the orientation distribution function (ODF, $f(g)$) was derived by use of a series expansion method ($l_{\text{max}} = 22$) [51]. Additionally the experimentally obtained textures were fitted by the texture component method [47].

Fig. 1 shows the microstructure of the as hot rolled ferritic steel in the surface and center layers. No substantial difference was found between the grain dimensions of the inspected layers. The grains in both layers are in part slightly elongated along RD and reveal an average grain size of 14.3 μm (ASTM 10).

Vickers hardness testing was conducted using a load of 98.1 N leading to HV10 hardness numbers. The average hardness amounted to 157.4 ± 0.75 HV10 on the surface and 168.1 ± 0.82 HV10 in the center layer. The mechanical properties were determined by tensile tests at 0° , 45° , and 90° relative to RD (Table 2). Three tensile specimens were probed for each direction to determine the mean value and the standard deviation.

4.2. Set-up of the finite element model and simulation details

The FE calculations were conducted under external plane strain boundary conditions to 95% engineering thickness reduction (logarithmic true strain $\varepsilon = 3.0$) by using MSC.Marc 2005 in conjunction with the user defined material subroutine HYPELA2. As the ferritic steel X6Cr17 is a bcc material, 24 slip systems ($12 \times \{110\}\langle 111 \rangle$ and $12 \times \{112\}\langle 111 \rangle$) were used for the simulations [2,14,38,45,52–

Table 1
Nominal chemical composition of X6Cr17 in wt.%

Fe	Cr	C	Si	Mn	P	S
Balance	16–18	<0.08	<1	<1	<0.40	<0.015

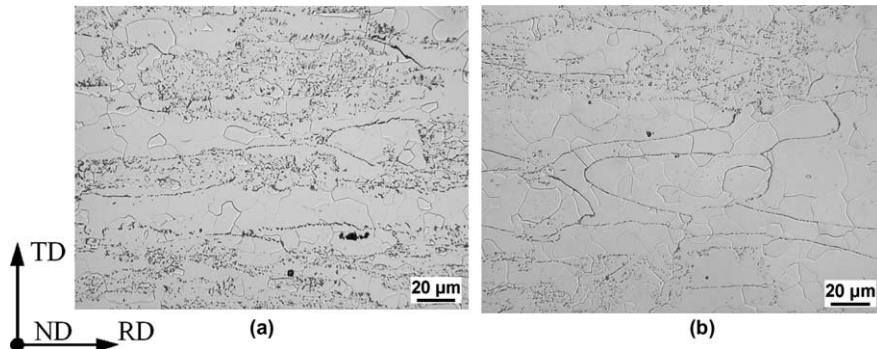


Fig. 1. Microstructure of the ferritic stainless steel X6Cr17 in flat sections; (a) surface layer ($s = 1.0$); (b) center layer ($s = 0.0$).

Table 2
Tensile properties of X6Cr17

RD	0°	45°	90°
$R_{p0.2}$ (MPa)	328.46	324.52	293.6
R_m (MPa)	514.79	512.89	491.36
A (%)	23.83	23.11	24.45
A_g (%)	15.74	16.24	16.58

[54]. The friction coefficients on the contact surface with the compression plane and the bottom surface were zero. The FE model consists of a set of 1152 3D linear elements each with eight nodes and eight integration points, Fig. 2. To consider the heterogeneity in terms of the through-thickness texture gradient of the hot band, one third of all elements, namely those in the center layers of the FE mesh, were occupied with the texture components fitted from the center layer. The two outer layers (top, bottom) were occupied with the texture components fitted for the surface.

Owing to the orthorhombic sample symmetry, each of the orientations has to be balanced by three additional symmetrically equivalent orientations in order to correctly reproduce the response of the material in the crystal plasticity FE calculations. Hardening of the ferritic stainless steel was described in terms of a set of adjustable parameters, where $\dot{\gamma}_0 = 0.001 \text{ s}^{-1}$ was used as reference value for the slip rate in the viscoplastic formulation [45,50]. The strain rate sensitivity parameter m was taken as 0.05. As hardening matrix parameters we used $q^{\alpha\beta} = 1.0$ for coplanar slip and $q^{\alpha\beta} = 1.4$ for non-coplanar slip. The components of the elasticity tensor were taken as $C_{11} = 230.1 \text{ GPa}$, $C_{12} =$

134.6 GPa, and $C_{44} = 116.6 \text{ GPa}$. The values of the slip system hardening parameters h_0 , a and s_s , and the initial value of the slip resistance s_0 were taken to be $h_0 = 180 \text{ MPa}$, $s_s = 148 \text{ MPa}$, $a = 2.25$, and $s_0 = 16 \text{ MPa}$.

5. Results and discussion

5.1. Experimental and recalculated hot rolling textures

It is known that for the prediction of deformation textures the correct incorporation of the starting texture is important [2,15]. The comparison of the recalculated $\{110\}$ and $\{200\}$ pole figures obtained from the texture component method with those which were experimentally determined for the surface and center layers are shown in Fig. 3. Besides the random texture portion eight components have to be used to approximate the experimental textures (Table 3). The recalculated textures show good agreement with the experimental pole figures although the overall pole density is somewhat weaker for the recalculated $\{111\}$ pole figures. The reason for this drop in the recalculated $\{111\}$ pole density might be that the texture component method has limited possibilities in the uniqueness of the approximation of minor portions of the experimental texture data. Fig. 4 shows the experimental starting textures for the surface layer (a) ($s = 1.0$), the center layer (b) ($s = 0.0$), and the integrated sample texture including the through-thickness texture gradient (c) ($1/3 \times s = 0.0$ and $2/3 \times s = 1.0$) in the form of $\varphi_2 = 45^\circ$ -sections through the Euler space as obtained from the model components. This type of ODF section reveals the orientation density both on the α_{bcc} -fiber ($\{110\}$ parallel to RD) and of the γ -fiber ($\{111\}$ parallel to ND).

The surface texture of the hot band specimen is comprised of a well pronounced and rather homogeneous γ -fiber with maximum values of $f(g)_{\text{max}} \approx 4.0$ near $\{111\}\langle 123 \rangle$ and $\{111\}\langle 112 \rangle$ and an incomplete α -fiber with strong rolling components near $\{001\}\langle 110 \rangle$ and $\{111\}\langle 110 \rangle$. The center layer texture shows a γ -fiber accompanied by the $\{111\}\langle 123 \rangle$ and $\{111\}\langle 112 \rangle$ orientations and the $\{112\}\langle 110 \rangle$ component which spreads out towards the $\{001\}\langle 110 \rangle$ orientation. Furthermore, an isolated $\{554\}\langle 225 \rangle$ component appears on the ε -fiber. The

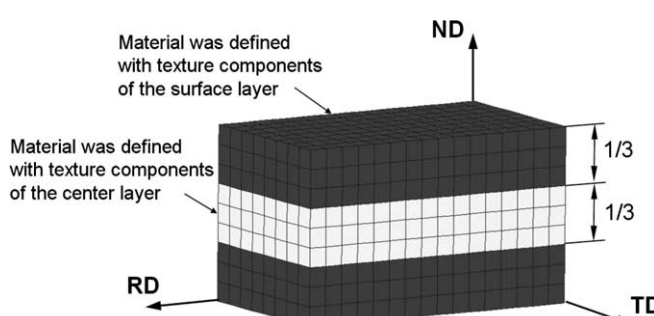


Fig. 2. Mapping of the through-thickness texture gradient in the FE mesh.

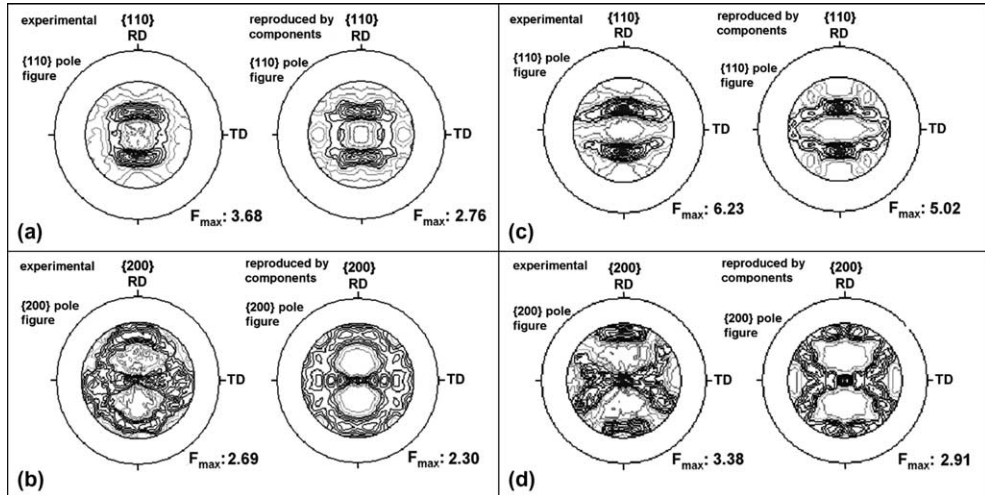


Fig. 3. The experimental and recalculated textures in terms of pole figures: (a) and (b) surface layer ($s = 1.0$), (c) and (d) center layer ($s = 0.0$).

Table 3
List of the texture components used for the model approximation

	φ_1 [°]	Φ [°]	φ_2 [°]	b	V (%)
<i>Surface layer ($s = 1.0$)</i>					
Comp. 1	314.1	130.2	135.2	18.9	26.05
Comp. 2	198.8	37.5	135.5	14.6	12.2
Comp. 3	261.6	91.1	112.7	12.6	7.54
Comp. 4	144.2	74.2	18.9	11.8	6.35
Comp. 5	308.7	57.3	40.2	11.6	7.19
Comp. 6	82.8	60.4	51.9	12.9	7.64
Comp. 7	320.9	97.5	82.2	6.7	2.84
Comp. 8	302.4	90.2	90.4	9.6	2.32
Random				27.89	
<i>Center layer ($s = 0.0$)</i>					
Comp. 1	211.4	118.0	118.9	13.4	23.97
Comp. 2	82.2	60.8	46.7	9.4	9.12
Comp. 3	122.9	68.2	22.5	10.5	7.95
Comp. 4	341.6	103.8	76.6	10.5	7.44
Comp. 5	250.3	60.3	46.3	13.6	5.43
Comp. 6	301.6	92.2	88.3	8.1	3.15
Comp. 7	295.3	95.1	88.4	16.5	2.59
Comp. 8	44.2	77.6	75.5	9.9	2.52
Random				37.83	

$\varphi_1, \Phi, \varphi_2$: Bunge–Euler angles; V : volume fraction; scatter width: b .

maximum orientation density of the center layer texture exceeds that observed in the surface layer by a factor of 1.3. The complete integrated texture, which includes 1/3 of the center layer texture ($s = 0.0$) and 2/3 of the surface layer texture ($s = 1.0$) is shown in Fig. 4c. It is similar to the texture of the surface ($s = 1.0$) layer which is an obvious result since two-thirds of the FE-model represent the surface texture components.

5.2. Simulation of the crystallographic texture by the TCCP-FE method during plane strain deformation

Fig. 5 documents the simulated texture evolution of the steel X6Cr17 during plane strain compression for 10%, 20%, 30%, 50%, 70%, 80% and 95% sample thickness reductions. The results for the surface, center, and the integrated sample including the through-thickness gradient are shown separately in each row. For up to 30% thickness reduction the simulated textures for the center layer ($s = 0.0$) and for the surface layer ($s = 1.0$) are similar to the starting texture.

Between 30% and 80% plane strain simulation, the decrease of the $\{111\}\langle 110 \rangle$ and $\{111\}\langle 112 \rangle$ components

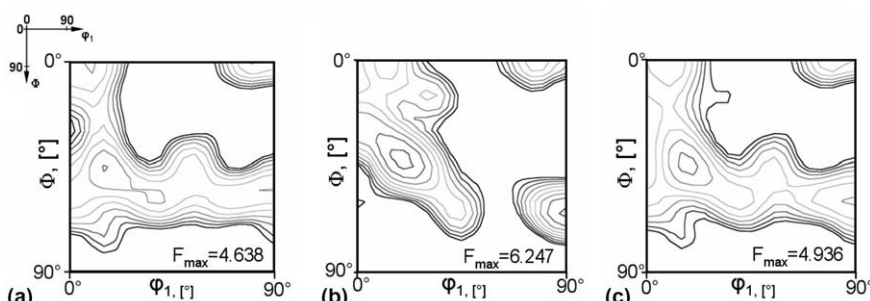


Fig. 4. Experimentally obtained starting texture of X6Cr17 in $\varphi_2 = 45^\circ$ sections (isoline levels 1, 2, 3, ..., 10): (a) surface layer ($s = 1.0$), (b) center layer ($s = 0.0$), (c) complete integrated sample texture including the through-thickness texture gradient.

on the γ -fiber and of the $\{001\}\langle 110 \rangle$ and $\{113\}\langle 110 \rangle$ components on the α -fiber occur both in the surface and center layer textures. Between 50% and 95% plane strain thickness reduction, the textures have become very similar in both layers ($s = 1.0$ and $s = 0.0$). After 95% plane strain compression both layers ($s = 1.0, s = 0.0$) display a pronounced $\{111\}\langle 112 \rangle$ component on the γ -fiber and strong rolling texture components near $\{112\}\langle 110 \rangle$ and $\{223\}\langle 110 \rangle$ on the α -fiber.

Moreover, the surface texture reveals in all rolling steps a slightly lower intensity than the center layer texture, so that also after 95% rolling a very weak texture gradient through the thickness remains visible. The integrated texture of the complete sample shows a rather similar development to that of the surface layer alone ($s = 1.0$).

When comparing these crystal plasticity FE texture simulations with corresponding experimental data taken from cold rolled samples of the hot band sheet which provided the starting data (Fig. 6) and also with similar rolling textures reported in the literature [2,5,7,19] one can observe a good agreement at small strains. However, some deviations between simulation and experiment become apparent at large strains above 70% thickness reduction. The first deviation for both through-thickness layers inspected is that the

experimental textures reveal a more continuous and fiber-type texture than the predicted ones. This applies both to the γ -fiber and to the α -fiber orientations. In particular the 45° rotated cube orientation, $\{001\}\langle 110 \rangle$, is more stable in the experiment than in the simulation. This effect may be attributed to the very sluggish recrystallization and rotation behavior which is typical of this texture component and which seems to root in particular in the in-grain microstructure of this orientation [3,15]. The second deviation is the relationship between the $\{111\}\langle 112 \rangle$ and the $\{111\}\langle 110 \rangle$ components on the γ -fiber. While the simulation predicts in both layers that the $\{111\}\langle 112 \rangle$ orientation is stronger than the $\{111\}\langle 110 \rangle$ orientation at large strains the experiment reveals the opposite tendency. This effect may be attributed to two reasons: The first one is the insufficient approximation of the experimentally observed textures with the texture component approximation. This is evident from the fitted texture components listed in Table 3 and the corresponding comparison of the experimental and the recalculated pole figures in Fig. 3. This problem associated with the texture component approximation of the ODF lies in the fact that with decreasing intensity in the pole figures or respectively in the difference pole figures some ambiguity enters the

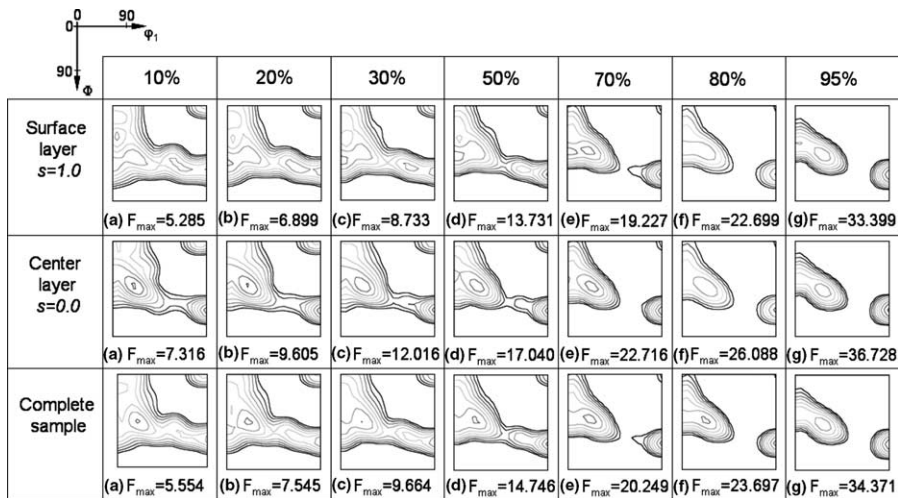


Fig. 5. Simulated texture evolution during cold rolling of X6Cr17 in $\varphi_2 = 45^\circ$ sections using 24 slip systems (isoline levels 1, 2, 3, ..., 10): (a)–(g) in first row: texture in surface layer ($s = 1.0$), (a)–(g) in second row: texture in center layer ($s = 0.0$), (a)–(g) in third row: integrated texture with through-thickness texture gradient.

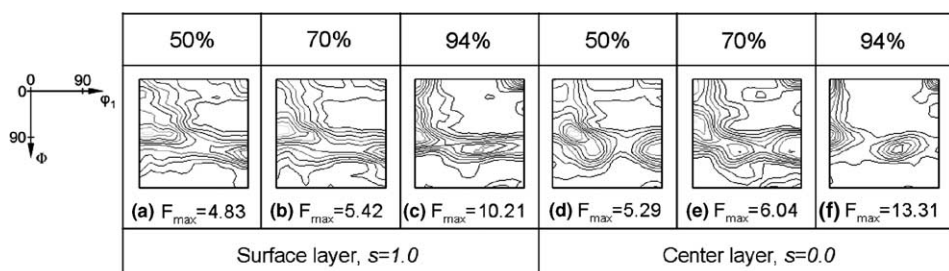


Fig. 6. Experimental cold rolling textures of X6Cr17 in the form of $\varphi_2 = 45^\circ$ sections (isoline levels 1, 2, 3, ..., 10): (a)–(c) texture in surface layer ($s = 1.0$), (d)–(f) texture in center layer ($s = 0.0$).

approximation procedure as to what texture component really improves the texture fit. An improved decomposition method to extract single orientations from an ODF and map those onto the integration points of a FE mesh might render the texture fit procedure more robust and less ambiguous when it comes to small orientation densities. The second possible reason for the deviations observed is the simplified approximation of the true hot band texture gradient between the abutting texture layers [15] in the FE-model. It is conceivable that a more appropriate mapping of the textures in the different layers in the FE model might yield an overall improved texture simulation.

6. Conclusions

The texture component crystal plasticity FE method was used for the simulation of the texture and of the texture gradient evolution during plane strain compression up to 95% thickness reduction of a ferritic stainless steel sheet X6Cr17. The material had a strong gradient in the starting texture which was inherited from the hot rolling process. The new simulation method accounts not only for the texture of the starting material but also for the texture development during forming. The integration of the method into commercial FEM software packages (MARC or ABQ) makes it easy to apply it to all kinds of starting microstructures, textures, and boundary conditions. In addition it allows one, as shown in this study, to conduct texture simulations under consideration of through-thickness texture gradients. Some deviations of the simulated texture evolution from experimental results observed at large rolling strains were attributed to two points: the first being the insufficient approximation of the true textures with the texture component fit method, and the second the insufficient mapping of the true texture gradient by the FE model.

Acknowledgement

We are grateful for the financial support of the Deutsche Forschungsgemeinschaft which is funding this study within the Schwerpunktprogramm 1138.

References

- [1] Houdremont E. Handbook of special steels. 3rd ed. Berlin: Springer Verlag; 1956. in German: Handbuch der Sonderstahlkunde.
- [2] Hölscher M, Raabe D, Lücke K. Acta Metall 1994;42:879.
- [3] Raabe D, Lücke K. Mater Sci Technol 1993;9:302.
- [4] Garbe S, Juul Jensen D, Poulsen HF, Krieger-Lassen NC, Raabe D. Mater Sci Forum 1998;273–275:271.
- [5] Fedosseev A, Raabe D, Gottstein G. Mater Sci Forum 1994;157–162:1771.
- [6] Raabe D, Lücke K. In: Ryan ND, Brown AJ, McQueen HJ, editors. Proceedings of international conference on strip casting, hot and cold working of stainless steels, Quebec, Canada, 1993, The Metall. Soc. CIM, p. 221.
- [7] Fedosseev A, Raabe D. Scripta Metall 1994;30:1.
- [8] Raabe D, Ylitalo M. Metall Mater Trans A 1996;27:49.
- [9] Raabe D, Lücke K. Mater Sci Forum 1994;157–162:597.
- [10] Raabe D. Mater Sci Technol 1995;11:461.
- [11] Raabe D. Mater Sci Technol 1995;11:985.
- [12] Raabe D, Ylitalo M. Metall Mater Trans A 1996;27:49.
- [13] Raabe D. J Mater Sci 1996;31:3839.
- [14] Tóth L, Molinari A, Raabe D. Metall Trans A 1997;28A:2343.
- [15] Raabe D. Steel Res 2003;74:327.
- [16] Raabe D, Lücke K. Scripta Metall 1992;26:19.
- [17] Raabe D, Lücke K. Steel Res 1992;63:457.
- [18] Raabe D, Lücke K. Scripta Metall Mater 1992;27:1533.
- [19] Hölscher M, Raabe D, Lücke K. Steel Res 1991;62:567.
- [20] Huh M-Y, Engler O. Mater Sci Eng A 2001;308:74.
- [21] Huh M-Y, Raabe D, Engler O. Steel Res 1995;66:353.
- [22] Park S, Kim K, Lee Y, Park C. ISIJ 2002;42:100.
- [23] Sheppard T, Richards P. Mater Sci Technol 1986;2:693.
- [24] Shin HJ, An JK, Park SH, Lee DN. Acta Mater 2003;51:4693.
- [25] Knutsen RD, Wittridge NJ. Mater Sci Technol 2002;18:1279.
- [26] Appel HG, Becker H. Z Metallkde 1963;54:724.
- [27] Engler O, Huh MY, Tome CN. Metall Mater Trans A 2005;36A:3127.
- [28] Wright SI, Gray GT, Rollet AD. Metall Mater Trans 1994;25A:1025.
- [29] Salsgiver JA, Larsen JM, Borneman PR. In: Chandra T editor. Proceedings of the international conference on recrystallisation'90, TMS, Warrendale (PA) 1990, p. 849.
- [30] Bethke K, Hölscher M, Lücke K. Mater Sci Forum 1994;157–162:1137.
- [31] Raabe D, Hölscher M, Reher F, Lücke K. Scripta Metall Mater 1993;29(1):113.
- [32] Raabe D, Hölscher M, Dubke M, Pfeifer H, Hanke H, Lücke K. Steel Res 1993;64:359.
- [33] Raabe D, Hölscher M, Dubke M, Reher F, Lücke K. Mater Sci Forum 1994;157–162:1039.
- [34] Raabe D, Krause H. In: Liang Z, Zuo L, Chu Y, editors. Proceedings of the 11th international conference on textures of materials ICOTOM 11, Sept. 16–20, 1996, Xi'an, China, International Academic Publishers, 137 Chaonei Dajie, Beijing 100010, China, ISBN 7-80003-376-7/TG.26, vol. 2, p. 854.
- [35] Raabe D, Krause H, Rollett AD, Teicher A. In: Jerzy A editor. Proceedings of the 12th international conference on textures of materials ICOTOM 12, Aug. 9–13, 1999, Montreal, Canada, Szpunar, NRC Research Press, National Research Council of Canada, Building M-55, Ottawa, ON K1A 0R6, Canada, 1999;2:1015.
- [36] Raabe D. Mater Sci Technol 1995;11:461.
- [37] Raabe D, Helming K, Roters F, Zhao Z, Hirsch J. Mater Sci Forum 2002;408–412:257.
- [38] Roters F, Jeon-Haurand HS, Raabe D. Mater Sci Forum 2005;495–497:937.
- [39] Raabe D, Roters F, Wang Y. Mater Sci Forum 2005;495–497:1529.
- [40] Zhao Z, Roters F, Mao W, Raabe D. Adv Eng Mater 2001;3:984.
- [41] Raabe D, Klose P, Engl B, Imlau K-P, Friedel F, Roters F. Adv Eng Mater 2002;4:169.
- [42] Raabe D, Roters F. Int J Plast 2004;20:339.
- [43] Zhao Z, Mao W, Roters F, Raabe D. Acta Mater 2004;52:1003.
- [44] Raabe D, Zhao Z, Roters F. Scripta Mater 2004;50:1085.
- [45] Raabe D, Wang Y, Roters F. Comput Mater Sci 2005;34:221.
- [46] Lücke K, Pospiech J, Jura J, Hirsch J. Z Metallkde 1986;312.
- [47] Helming K, Schwarzer RA, Rauschenbach B, Geier S, Leiss B, Wenk H, et al. Z Metallkde 1994;85:545.
- [48] Raabe D, Lücke K. Phys Status Solidi (B) 1993;180:59.
- [49] Raabe D, Lücke K. Mater Sci Forum 1994;157–162:413.
- [50] Kalidindi SR, Bronkhorst CA, Anand L. J Mech Phys Solids 1992;40:537.
- [51] Bunge HJ. Texture analysis in materials science. London: Butterworths; 1982.
- [52] Raabe D. Mater Sci Eng A 1995;197:31.
- [53] Raphanel JL, Van Houtte P. Acta Metall 1985;33:1481.
- [54] Van Houtte P, Delannay L, Samajdar I. Text Microstruct 1999;31:109.